nature genetics

DYX1C1 is required for axonemal dynein assembly and ciliary motility

Aarti Tarkar[1,20], Niki T Loges[2,20], Christopher E Slagle[3,20], Richard Francis[4], Gerard W Dougherty[2], Joel V Tamayo[3], Brett Shook[1], Marie Cantino[1], Daniel Schwartz[1], Charlotte Jahnke[2], Heike Olbrich[2], Claudius Werner[2], Johanna Raidt[2], Petra Pennekamp[2], Marouan Abouhamed[2], Rim Hjeij[2], Gabriele Köhler[5], Matthias Griese[6], You Li[4], Kristi Lemke[4], Nikolas Klena[4], Xiaoqin Liu[4], George Gabriel[4], Kimimasa Tobita[4], Martine Jaspers[7], Lucy C Morgan[8], Adam J Shapiro[9], Stef J F Letteboer[10,11], Dorus A Mans[10,11], Johnny L Carson[9], Margaret W Leigh[9], Whitney E Wolf[12], Serafine Chen[3], Jane S Lucas[13], Alexandros Onoufriadis[14], Vincent Plagnol[15], Miriam Schmidts[14], Karsten Boldt[16], UK10K[17], Ronald Roepman[10,11,18], Maimoona A Zariwala[19], Cecilia W Lo[4], Hannah M Mitchison[14], Michael R Knowles[12], Rebecca D Burdine[3], Joseph J LoTurco[1,21] & Heymut Omran[2,21]

***DYX1C1* has been associated with dyslexia and neuronal migration in the developing neocortex. Unexpectedly, we found that deleting exons 2–4 of *Dyx1c1* in mice caused a phenotype resembling primary ciliary dyskinesia (PCD), a disorder characterized by chronic airway disease, laterality defects and male infertility. This phenotype was confirmed independently in mice with a *Dyx1c1* c.T2A start-codon mutation recovered from an *N*-ethyl-*N*-nitrosourea (ENU) mutagenesis screen. Morpholinos targeting *dyx1c1* in zebrafish also caused laterality and ciliary motility defects. In humans, we identified recessive loss-of-function *DYX1C1* mutations in 12 individuals with PCD. Ultrastructural and immunofluorescence analyses of DYX1C1-mutant motile cilia in mice and humans showed disruptions of outer and inner dynein arms (ODAs and IDAs, respectively). DYX1C1 localizes to the cytoplasm of respiratory epithelial cells, its interactome is enriched for molecular chaperones, and it interacts with the cytoplasmic ODA and IDA assembly factor DNAAF2 (KTU). Thus, we propose that DYX1C1 is a newly identified dynein axonemal assembly factor (DNAAF4).**

Cilia, hair-like organelles projecting from the surface of nearly all polarized cell types, serve essential roles in cellular signaling and motility[1]. The basic structure of motile cilia and the related organelle flagella is evolutionarily conserved. In most motile cilia, a ring of nine peripheral microtubule doublets surrounds a central pair apparatus of single microtubules that connect to the nine peripheral doublets by radial spokes (9+2 structure). Motile monocilia present at the mouse node during early embryogenesis are an exception, lacking the central pair apparatus (9+0 structure). Distinct multiprotein dynein complexes attached at regular intervals to the peripheral microtubule doublets contain molecular motors that drive and regulate ciliary motility. Specifically, ODAs are responsible for beat generation, whereas both the IDAs and the nexin link–dynein regulatory complexes (N-DRCs) regulate ciliary and flagellar beating pattern and frequency. Identifying the proteins responsible for the correct assembly of this molecular machinery is critical to understanding the causes of motile cilia–related diseases.

PCD (MIM 244400), a rare genetic disorder affecting approximately 1 in 20,000 individuals, is caused by immotile or dyskinetic cilia. Loss of ciliary function in upper and lower airways causes defective

[1]Department of Physiology and Neurobiology, University of Connecticut, Storrs, Connecticut, USA. [2]Department of Pediatrics, University Hospital Münster, Münster, Germany. [3]Department of Molecular Biology, Princeton University, Princeton, New Jersey, USA. [4]Department of Developmental Biology, University of Pittsburgh School of Medicine, Pittsburgh, Pennsylvania, USA. [5]Department of Pathology, University Hospital Münster, Münster, Germany. [6]Department of Pediatrics, Dr. von Hauner Children's Hospital, Ludwig-Maximilians University, Munich, Germany. [7]Department of Otorhinolaryngology, University Hospital Leuven, Leuven, Belgium. [8]Department of Respiratory Medicine, Concord Hospital, Concord, New South Wales, Australia. [9]Department of Pediatrics, University of North Carolina (UNC) School of Medicine, Chapel Hill, North Carolina, USA. [10]Department of Human Genetics, Radboud University Medical Centre, Nijmegen, The Netherlands. [11]Nijmegen Centre for Molecular Life Sciences, Radboud University Medical Centre, Nijmegen, The Netherlands. [12]Department of Medicine, UNC School of Medicine, Chapel Hill, North Carolina, USA. [13]Primary Ciliary Dyskinesia Centre, National Institute for Health Research (NIHR) Southampton Respiratory Biomedical Research Unit, University of Southampton and University Hospital Southampton National Health Service (NHS) Foundation Trust, Southampton, UK. [14]Molecular Medicine Unit, Institute of Child Health, University College London, London, UK. [15]Genetics Institute, University College London, London, UK. [16]Institute for Ophthalmic Research, Division of Experimental Ophthalmology and Medical Proteome Center, University of Tübingen, Tübingen, Germany. [17]Details appear in the **Supplementary Note**. [18]Institute for Genetic and Metabolic Disease, Radboud University Medical Centre, Nijmegen, The Netherlands. [19]Department of Pathology & Laboratory Medicine, UNC School of Medicine, Chapel Hill, North Carolina, USA. [20]These authors contributed equally to this work. [21]These authors jointly directed this work. Correspondence should be addressed to J.J.L. (joseph.loturco@uconn.edu) or H. Omran (heymut.omran@ukmuenster.de).

Received 5 April; accepted 24 June; published online 21 July 2013; doi:10.1038/ng.2707

mucociliary airway clearance and, subsequently, chronic inflammation that regularly progresses to destructive airway disease (bronchiectasis). Organ laterality defects are also observed, with approximately half of individuals with PCD exhibiting *situs inversus* and, more rarely, *situs ambiguus*, which can associate with complex congenital heart disease[2]. Dysfunctional sperm tails (flagella) frequently cause male infertility in individuals with PCD. Another consequence of ciliary dysfunction, particularly evident in mouse models, is hydrocephalus caused by disrupted flow of cerebrospinal fluid through the cerebral aqueduct connecting the third and fourth brain ventricles[3]. Although ciliary dysmotility is not sufficient for hydrocephalus formation in humans owing to morphological differences between the mouse and human brains, the incidence of hydrocephalus, secondary to aqueduct closure, is higher in individuals with PCD[3].

Genetic analyses of individuals with PCD have identified several autosomal recessive mutations in genes encoding axonemal subunits of the ODA complexes and related components[4–12]. In addition, recessive mutations in *CCDC39* (MIM 613798) and *CCDC40* (MIM 613799) have been linked to PCD with severe tubular disorganization and defective nexin links[13,14]. Mutations in the radial spoke head genes *RSPH4A* and *RSPH9* as well as in *HYDIN* can cause intermittent or complete loss of the central-apparatus microtubules[15–17]. Two X-linked PCD variants associated with syndromic cognitive dysfunction and retinal degeneration are caused by mutations in *OFD1* (MIM 311200) and *RPGR* (MIM 312610), respectively[18,19]. Another functional class of proteins emerging from the identification of PCD-causing mutations are proteins involved in the cytoplasmic preassembly of both ODAs and IDAs, including those encoded by *DNAAF2* (also known as *KTU*; MIM 612517)[20], *DNAAF1* (also known as *LRRC50*; MIM 613190)[21,22], *DNAAF3* (also known as *C19orf51*; MIM 614566)[23] and the recently identified *LRRC6* (MIM 614930)[24].

DYX1C1 (MIM 608706) was initially identified as a candidate dyslexia gene, owing to both a single balanced translocation t(2;15)(q11;q21) coincidentally segregating with dyslexia in a family[25] and subsequent SNP association studies. Follow-up gene association studies have provided both positive[26–28] and negative[29–31] support for association with dyslexia. Molecular and cellular analyses of DYX1C1 have indicated potential functional roles with chaperonins[32,33] and in estrogen receptor trafficking[34] and neuronal migration[35,36], and recent proteomic and gene expression studies have suggested a possible role in cilia[37,38].

RESULTS

Generation of *Dyx1c1*-mutant mice

To elucidate the biological functions of DYX1C1, we performed a forward genetic experiment by producing an allele of *Dyx1c1* in mice in which exons 2–4 were deleted (**Fig. 1a**). Homozygous mutant mice ($Dyx1c1^{\Delta/\Delta}$) expressed no detectable DYX1C1 protein by immunoblot analysis of all tissues tested, including brain and lung (**Fig. 1b**). Mice heterozygous for the deletion allele were viable, fertile and not noticeably different from wild-type littermates. Homozygous mutant mice were recovered after birth from heterozygous breeding pairs at a rate deviating from the expected mendelian ratio (295:570:87 for $Dyx1c1^{+/+}$:$Dyx1c1^{\Delta/+}$:$Dyx1c1^{\Delta/\Delta}$, $\chi = 128.017$, $P < 0.0001$) but were recovered at early embryonic times (embryonic day (E) 6.5–12) at the expected mendelian ratio (22:43:20, $\chi = 0.105$, $P = 0.85$), suggesting embryonic lethality of approximately two-thirds of homozygous mutants. Homozygous mutants that survived after birth developed severe hydrocephalus by postnatal day (P) 16 (**Fig. 1c**) and died by P21, similar to what has been described for other mouse mutants with defective motile cilia[3,39].

In addition to hydrocephaly, postnatal homozygous mutant mice displayed laterality defects, with 59% of mutants (51/87) showing

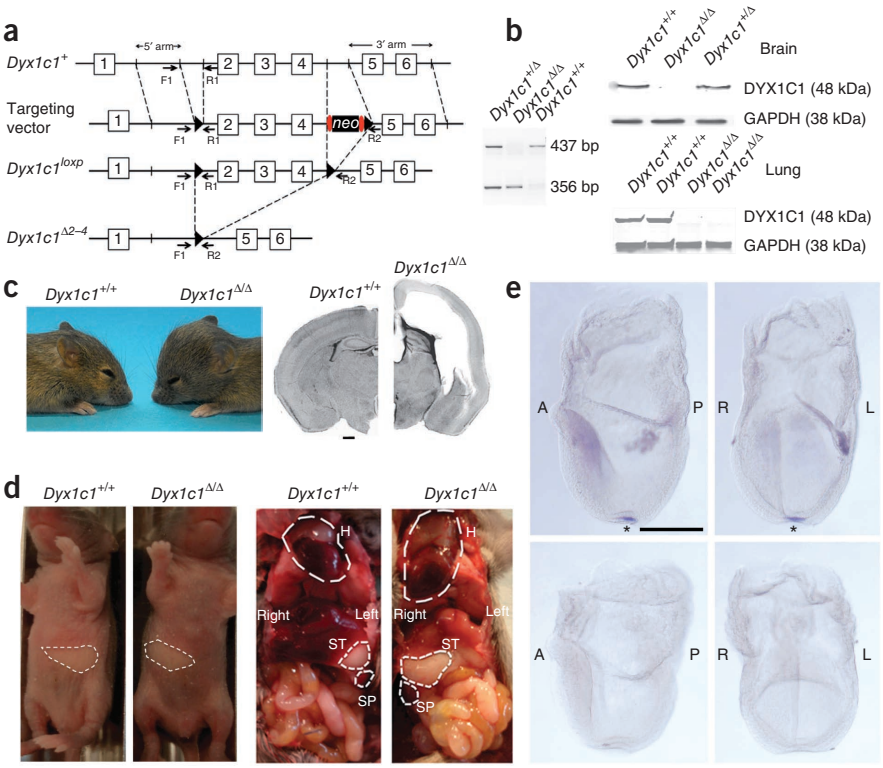

Figure 1 Deficiency of *Dyx1c1* in mouse causes phenotypes consistent with motile cilia defects. (**a**) Schematic of the strategy for producing the *Dyx1c1* exon 2–4 deletion allele. We created a conditional knockout allele by homologous recombination and deleted exons 2–4 from the germ line by breeding mice to an *Hprt-cre* line. (**b**) Left, PCR showing the genotyping results for the wild-type (genotyping primers forward 1, F1, and reverse 1, R1, 437 bp) and deletion (genotyping primers forward 1, F1, and reverse 2, R2, 356 bp) alleles. Right, protein blots showing the presence of DYX1C1 protein detected in the brain and lung of wild-type ($Dyx1c1^{+/+}$) and heterozygous ($Dyx1c1^{+/\Delta}$) animals but missing from homozygous mutants ($Dyx1c1^{\Delta/\Delta}$). (**c**) Evidence of hydrocephalus in $Dyx1c1^{\Delta/\Delta}$ mice. The characteristic domed crown in $Dyx1c1^{\Delta/\Delta}$ mice develops by P16, with the ventricles seen in coronal sections greatly expanded in $Dyx1c1^{\Delta/\Delta}$ relative to $Dyx1c1^{+/+}$ mice. Scale bar, 250 µm. (**d**) *Situs inversus* in $Dyx1c1^{\Delta/\Delta}$ mice as seen in both the reversal of the milk-filled stomach in neonates to the right side and exposed viscera showing reversal of multiple organs, including heart (H), stomach (ST) and spleen (SP). The positions of the relevant organs are highlighted by dashed circles. (**e**) Whole-mount *in situ* hybridization analysis of *Dyx1c1* in mouse embryos at E7.5. *Dyx1c1* expression is restricted to the pit cells of the ventral node (top: *Dyx1c1* antisense probe, an asterisk marks the location of the node; bottom: *Dyx1c1* sense control probe; left: lateral view from the left; right: frontal view). A, anterior; L, left; P, posterior; R, right. Scale bar, 500 µm.

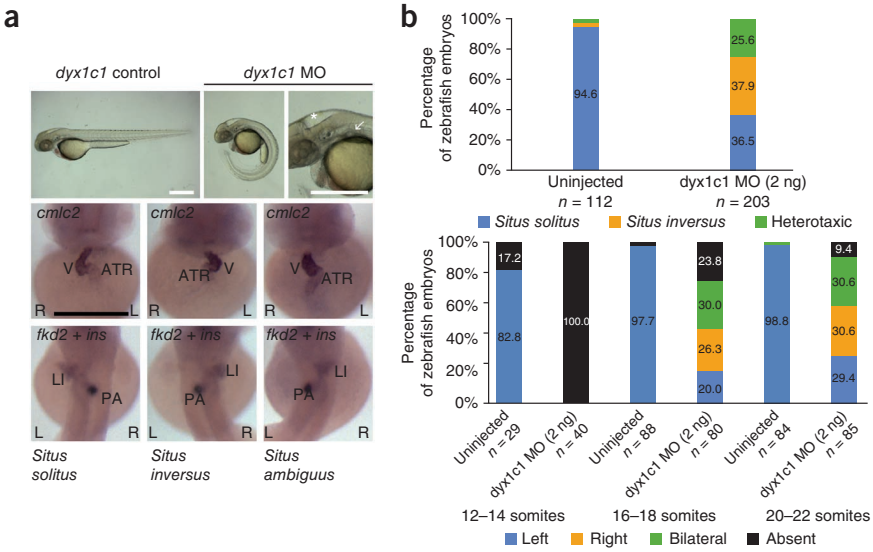

Figure 2 Knockdown of *dyx1c1* in zebrafish. (**a**) Phenotypes of zebrafish embryos 48 h.p.f., with AUG-targeting morpholinos (MOs) injected between the one- and four-cell stages. Top, lateral images of wild-type and *dyx1c1*-morphant zebrafish embryos at 48 h.p.f. The morphants have a curly tail down phenotype and exhibit hydrocephalus (asterisk in enlarged image) as well as pronephric cysts (arrow in enlarged image). Ventral views of the heart (middle) and dorsal views of the liver and pancreas (bottom) are shown in *dyx1c1*-morphant embryos at 48 h.p.f. The heart, liver and pancreas were visualized by *in situ* hybridization for *cmlc2*, *fkd2* and *ins*, respectively. L, left; R, right; V, ventricle; ATR, atrium; LI, liver; PA, pancreas. Scale bars, 500 μm. (**b**) Top, graph showing the defects in visceral asymmetry in *dyx1c1*-morphant embryos compared to uninjected controls 48 h.p.f. Laterality defects are associated with 2 ng of *dyx1c1* AUG-targeting morpholinos. Bottom, graph showing alterations in the asymmetric gene expression of *spaw* in the LPM of *dyx1c1* morpholino–injected embryos compared to uninjected controls at three developmental stages between 15–20 h.p.f.

situs inversus totalis (a complete inversion of left-right asymmetry; **Fig. 1d**), 17% (15/87) showing *situs ambiguous* with inverted heart and lung position relative to stomach and spleen or inverted stomach and spleen position relative to heart and lung, and 24% (21/87) showing *situs solitus* (normal left-right asymmetry). Mutations that cause disruptions in left-right asymmetry in mice[40] are known to result from defects in the function of motile nodal monocilia and, more specifically, the loss of cilia-generated leftward flow across the node in early embryogenesis[40]. The typical phenotype for laterality mutants is a 1:1 ratio of *situs inversus totalis* and *situs solitus*, indicating a randomization of left-right patterning, although the *inv* mutant mouse has 100% of affected pups with *situs inversus*. Even if the ratio of *situs inversus* to *situs solitus* seen in surviving *Dyx1c1*-mutant mice deviates significantly from what would be expected for a 1:1 ratio of *situs inversus* to *situs solitus* (51:21, $\chi = 12.5$, $P = 0.0004$), this ratio was already observed in other mutants for left-right patterning, such as in *Dnahc5*-mutant mice[41]. Consistent with a role for DYX1C1 function in the embryonic node where left-right patterning is established in the mouse, we found by whole-mount *in situ* hybridization that *Dyx1c1* expression in the early embryo (E7.5) was restricted to pit cells of the embryonic node (**Fig. 1e**).

In an independent mouse ENU mutagenesis screen for congenital heart defects (CHDs) of the National Heart, Lung, and Blood Institute (NHLBI) Bench to Bassinet Program, we recovered a mutant named *Sharpei* with a *Dyx1c1* missense mutation (c.T2A) that resulted in an altered AUG start codon and expression of an aberrant N-terminally truncated DYX1C1 protein product of approximately 31 kDa (**Supplementary Fig. 1a**). This mutant was recovered on the basis of having a complex CHD and was therefore carefully histologically phenotyped. Some mutants with apparent *situs inversus* comprising dextrocardia with inverted lung lobation and right-sided stomach also had subtle visceral organ situs defects, such as discordant left-sided pancreas and spleen, despite right-sided stomach positioning (**Supplementary Fig. 1b**). *Sharpei* mutants with complex CHD died prenatally or at birth with a spectrum of defects, such as transposition of the great arteries with ventricular septal defect (VSD) and coronary fistula (**Supplementary Fig. 1b** and **Supplementary Video 1**) or double-outlet right ventricle with right atrial isomerism, muscular and atrioventricular septal defects (**Supplementary Fig. 1b** and **Supplementary Videos 2** and **3**). All these findings resemble CHDs observed in other mouse models of PCD such as *Dnahc5*-mutant mice[41].

Knockdown of *dyx1c1* in zebrafish

Recently, it was shown that knockdown of *dyx1c1* results in phenotypes characteristically associated with cilia defects, such as body curvature, hydrocephalus, cystic kidneys and *situs inversus*[42]. To test whether DYX1C1 has an evolutionarily conserved role in establishing left-right asymmetry in vertebrates, we also performed morpholino-mediated knockdown experiments in zebrafish embryos. In zebrafish, *dyx1c1* is expressed in embryonic tissues that contain motile cilia[42], including Kupffer's vesicle, which is known to have an important role in establishing the left-right axis. Morpholino-mediated knockdown of zebrafish *dyx1c1* resulted in hydrocephalus, kidney cysts and body-axis curvature, phenotypes consistent with ciliary dysfunction in zebrafish. Morpholino-mediated knockdown of *dyx1c1* also produced laterality defects (**Fig. 2a**,**b**), as assessed by the position of the heart (*cmlc2*), liver (*fkd2*) and pancreas (*ins*) in *dyx1c1*-morphant embryos at 48 h post-fertilization (h.p.f.). In a wild-type zebrafish embryo, the ventricle of the heart loops toward the right, the atrium loops toward the left, the liver is positioned to the left of the midline and the pancreas lies to the right of the midline (**Fig. 2a**). We observed this wild-type pattern in 36.5% of the morphants, whereas 37.9% of the morphants showed a complete reversal of the placement of these organs (**Fig. 2b**). A heterotaxic (or *situs ambiguus*) phenotype was seen in 25.6% of the embryos (**Fig. 2b**). To investigate when *dyx1c1* affects early left-right patterning, we studied the expression of the zebrafish nodal gene *southpaw* (*spaw*) in a time course of morpholino-injected embryos. The expression of zebrafish *spaw* is restricted to the left lateral-plate mesoderm (LPM) during somitogenesis before asymmetric organ positioning at 48 h.p.f. (ref. 43). At the 12- to 14-somite stage, 82.8% of the control embryos had left LPM expression of *spaw*, whereas all of the morphant embryos lacked any expression of *spaw*, indicating that *spaw* initiation is delayed in the absence of *dyx1c1* (**Fig. 2b**). The delay in *spaw* expression upon loss of ciliary motility in Kupffer's vesicle

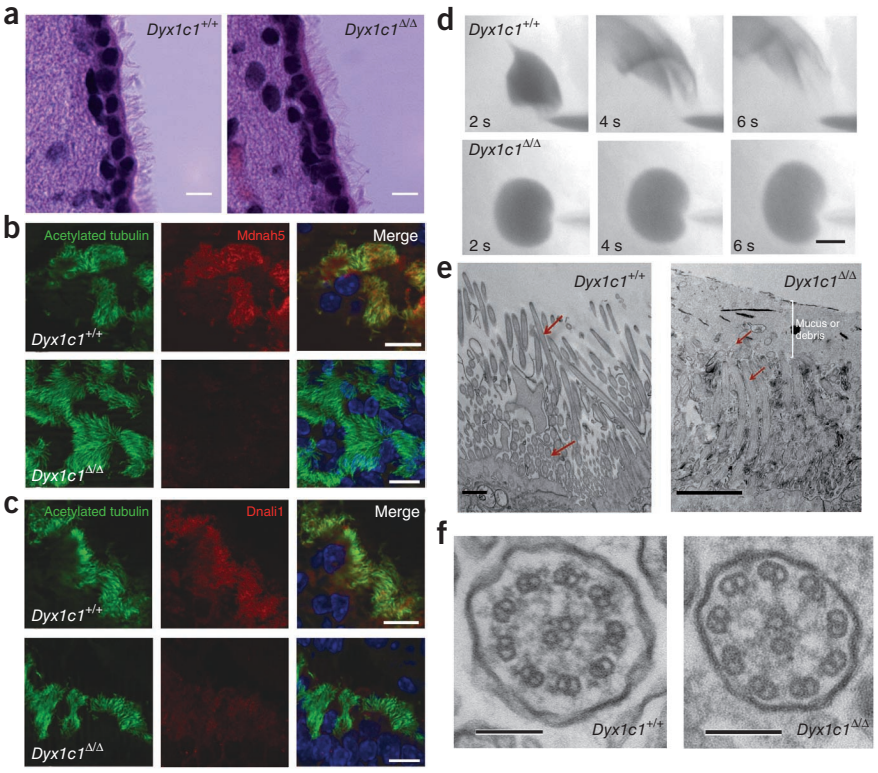

Figure 3 Motile cilia are dysfunctional in *Dyx1c1*-mutant mice. (**a**) Sections of the cerebral ventricles stained with hematoxylin and eosin show the presence of cilia on the surface of the ependymal cells in both *Dyx1c1*$^{+/+}$ and *Dyx1c1*$^{\Delta/\Delta}$ mice. (**b**,**c**) Immunofluorescence analyses of lung sections stained for acetylated tubulin along with ODA heavy chain Mdnah5 (**b**) and IDA light chain Dnali1 (**c**). Nuclei were stained with DAPI. In contrast to *Dyx1c1*$^{+/+}$ mice, in which Mdnah5 and Dnali1 colocalized with acetylated tubulin (top in **b**,**c**), in *Dyx1c1*$^{\Delta/\Delta}$ mice, Mdnah5 and Dnali1 (bottom in **b**,**c**) were completely absent from ciliary axonemes. (**d**) Flow of fluid (India ink) across the ependymal surface in brain ventricle cup preparations from *Dyx1c1*$^{+/+}$ and *Dyx1c1*$^{\Delta/\Delta}$ mice at P6. Directional flow was rapid across the surface of *Dyx1c1*$^{+/+}$ ependymal epithelia, whereas only non-directional passive diffusion was observed on ependymal surfaces in *Dyx1c1*$^{\Delta/\Delta}$ mice. The starting point for the fluid is at the end of the pipette tip, seen bottom right. (**e**) TEM images of cross-sections through the trachea of *Dyx1c1*$^{+/+}$ and *Dyx1c1*$^{\Delta/\Delta}$ mice. Abundant cilia were present in each, but cilia structures (red arrows) in the *Dyx1c1*$^{\Delta/\Delta}$ trachea are surrounded by cellular debris and mucus. (**f**) TEM cross-section images of ependymal and tracheal cilia in *Dyx1c1*$^{+/+}$ and *Dyx1c1*$^{\Delta/\Delta}$ mice. The 9+2 microtubular structure was well preserved in *Dyx1c1*$^{\Delta/\Delta}$ mice, except that the ODAs and IDAs were lacking in tracheal cilia. Scale bars, 10 μm in **a**–**d**, 1 μm (left) and 2 μm (right) in **e**, 0.1 μm in **f**.

has not been reported previously but has been observed in other ciliary motility mutants in which the structure of Kupffer's vesicle is not affected (J. McSheene and R.D.B., unpublished data). At the 16- to 18-somite and 20- to 22-somite stages, most of the control embryos (97.7% and 98.8%, respectively) had *spaw* expression in the left LPM, but the morphants displayed a randomized expression pattern, in which expression was bilateral (30 and 30.6%), left-sided (20 and 29.4%), right-sided (26.3 and 30.6%) or absent (23.8 and 9.8%) (**Fig. 2b**). Thus, in the zebrafish embryo, *dyx1c1* is necessary for the left-sided expression of *spaw* in the left LPM, which is a crucial step for normal left-right axis development. Overall, our results confirm previous findings[42]. Furthermore, we demonstrate that knockdown of *dyx1c1* affects the left-sided expression of *spaw*, consistent with a key role for this factor in left-right axis development.

Analysis of ependymal cilia

Hydrocephalus and organ laterality defects are hallmarks of mutations that cause defects in ciliary motility in mice and zebrafish[1,3]. We therefore used light and electron microscopy as well as videomicroscopy to determine whether DYX1C1 deficiency caused loss of motile cilia formation or loss of cilia. Cilia extending from mouse ependymal cells of the cerebral ventricles, visualized by light microscopy, appeared similar in length and distribution in *Dyx1c1*$^{\Delta/\Delta}$ and wild-type littermates (**Fig. 3a**). Although cilia were abundant on respiratory epithelial cells in mutants and wild-type mice, cilia in mutants lacked immunofluorescence signal for both the ODA heavy chain Mdnah5 and the IDA light chain Dnali1 proteins (**Fig. 3b**,**c**). Loss of these dyneins from motile cilia would be predicted to cause a loss of motility. We used live-cell imaging to directly assess cilia-mediated fluid flow and ciliary motility on the ependymal surface in *Dyx1c1*$^{\Delta/\Delta}$ mice. We prepared explants or slices of the lateral ventricular surfaces from *Dyx1c1*$^{\Delta/\Delta}$ and wild-type mice at P6. Ependymal cilia in wild-type mice continued to beat vigorously in these preparations and created a directional fluid flow across the surface that could be visualized by the displacement of a small volume of India ink pressure-injected onto the ependymal surface. This flow was present in all wild-type mice tested (n = 6; **Fig. 3d** and **Supplementary Video 4**) but was completely absent in tissue obtained from all *Dyx1c1*$^{\Delta/\Delta}$ mice tested (n = 4; **Fig. 3d** and **Supplementary Video 5**). We next examined the motility of ependymal cilia in coronal brain slices of wild-type and *Dyx1c1*$^{\Delta/\Delta}$ mice by infrared differential interference contrast (DIC) videomicroscopy. Cilia at the ependymal surface in wild-type and heterozygous mice (n = 8) were found to beat at a frequency of approximately 9 beats/s (34 °C; **Supplementary Video 6**), whereas cilia on ependymal cells from all *Dyx1c1*$^{\Delta/\Delta}$ examined (n = 4) lacked ciliary beating (**Supplementary Video 7**). Videomicroscopy of tissue slices from the third brain ventricle in newborn homozygous *Sharpei* mutants also showed completely immotile cilia (n = 7; **Supplementary Video 8**). Beads added to the solution above the brain slice exhibited only random motion, whereas, in wild-type littermate controls, the beads showed ependymal cilia–generated flow (**Supplementary Video 8**). Similarly, videomicroscopy of the tracheal airway epithelia in newborn homozygous *Sharpei* mutants showed completely immotile cilia, consistent with PCD, whereas littermate controls showed normal rapid synchronous ciliary beat (**Supplementary Video 9**). We also assessed the motility of cilia in Kupffer's vesicle in *dyx1c1*-morphant zebrafish with videomicroscopy. *dyx1c1* morphants had cilia in Kupffer's vesicles that lacked motility compared to the cilia in uninjected embryos (**Supplementary Videos 10** and **11**).

Analysis of *Dyx1c1*-mutant respiratory cilia

To assess the ultrastructure of respiratory cilia in mutants, we obtained transmission electron micrographs of tracheal cilia. As on the ependymal surface, tracheal cilia were abundant in both wild-type and *Dyx1c1*$^{\Delta/\Delta}$ epithelial cells (**Fig. 3e**), but, unlike tracheal cilia in wild-type mice, cilia in the *Dyx1c1*$^{\Delta/\Delta}$ trachea were surrounded by cellular debris and mucus (**Fig. 3e**). We further examined the ultrastructure of tracheal cilia in cross-sections by transmission electron microscopy (TEM). Using TEM, we observed that tracheal cilia in wild-type and mutant mice had typical 9+2 microtubular structure with intact radial spokes (**Fig. 3f**). In contrast and consistent with the absence of heavy and light chain dynein subunits (**Fig. 3b**), cilia in *Dyx1c1*$^{\Delta/\Delta}$ mice lacked both ODA and IDA structures in respiratory cilia (**Fig. 3f**). Thus, the phenotype caused by loss of function of *Dyx1c1* is a severe ciliary motility defect associated with absent axonemal ODA and IDA structures.

Mutation analysis of *DYX1C1* in individuals with PCD

The apparent conservation of function of DYX1C1 in mice and zebrafish prompted us to search for mutations in *DYX1C1* in humans with PCD, the disorder connected with defective ciliary motility. Because of the observed ultrastructural phenotype and severe ciliary beating defect in *Dyx1c1*$^{\Delta/\Delta}$ mice, we considered *DYX1C1* an excellent candidate gene for PCD with abnormal axonemal ODA and IDA assembly. *DYX1C1*, located on chromosome 15q21.3, comprises ten exons (translation starts in exon 2) and encompasses 77.93 kb of genomic DNA. In one highly inbred Irish family (UCL-200), a copy number variation (CNV) analysis of whole-exome sequence data (using ExomeDepth)[44] identified a homozygous *DYX1C1* deletion in two affected siblings (UCL-200 II:1 and UCL-200 II:2; **Supplementary Fig. 2a**,**b**). This finding was confirmed by Sanger sequencing of the deletion breakpoints, and the deletion was present in a heterozygous state in their carrier mother (**Supplementary Fig. 2c**). The 3.5-kb deletion led to loss of exon 7 of *DYX1C1* (**Fig. 4a**). Notably, the same 3.5-kb deletion was also identified in individuals with PCD in five US and Australian families. Five of these individuals were heterozygous for the deletion along with a mutation in the splice donor site of exon 6, stop-gain mutations and a frameshift mutation in the other allele (UNC-158, UNC-159, UNC-1669, UNC-1839 and UNC-1171; **Fig. 4a** and **Supplementary Fig. 3e**–**h**), and one individual was homozygous for the deletion (UNC-663; **Supplementary Fig. 3i**). In addition, we screened all *DYX1C1* exons and adjacent intronic sequences by PCR amplification and subsequent Sanger DNA sequencing in 105 individuals with PCD with combined ODA and IDA defects. Mutations were identified in ten affected individuals from nine unrelated families that predicted premature termination of translation (**Fig. 4a**,**b** and **Supplementary Table 1**). In all families, the mutations segregated with disease status, consistent with an autosomal recessive inheritance pattern (**Supplementary Figs. 2** and **3**). In three families, we confirmed recessively inherited homozygous mutations by sequencing other family members (F648 II1, OP-359 II1 and OP-556 II1). In another family, the affected individual, OP-86 II2, was compound heterozygous for two different mutations, with each mutation tracking uniquely to one of parent (**Supplementary Fig. 3a**). We therefore identified a total of nine human *DYX1C1* mutations (**Supplementary Table 1**). Apart from the 3.5-kb deletion and a splice-site mutation, the other seven mutations were predicted to cause premature protein termination and clustered toward the middle of the 420-amino-acid sequence, between amino acids 128 and 195 (**Fig. 4b**). Thus, seven of the nine identified mutations are predicted to result in a truncated DYX1C1 protein that would lack more than half of the protein, including the C-terminal tetratricopeptide-repeat (TPR) domain. The TPR domains in DYX1C1 have been shown previously to be functionally important domains required for the activities of DYX1C1 in neuronal motility, its cellular localization and its interaction with molecular chaperones[33,35].

Clinical phenotypes of individuals with *DYX1C1* mutations

All 12 individuals with biallelic *DYX1C1* mutations suffered from classical symptoms of PCD, including recurrent upper and lower airway disease and bronchiectasis. Seven had neonatal respiratory distress syndrome. Four exhibited reduced fertility (**Supplementary Table 1**), and one male subject was treated for infertility, having three children by assisted reproduction, suggesting a probable function for DYX1C1 in sperm tails. Five of the 12 affected individuals had *situs inversus totalis* (42%), 2 had *situs ambiguous* (16%), 1 with dextrocardia and polysplenia and 1 with left atrial isomerism and polysplenia, and 5 had *situs solitus* (42%). Thus, *DYX1C1* deficiency in humans causes disruption of left-right body asymmetry, similar to the findings observed in mice and zebrafish. Notably, none of these individuals were diagnosed with dyslexia or hydrocephaly. Hydrocephalus is a common phenotype in mouse mutants with immotile cilia but is rare in humans with PCD[3,39]. Two affected individuals in this study had a learning disability, but this phenotype can probably be attributed to other causes, including microcephaly (OP-86 II2 and UCL-200 II:1).

Dynein-arm defects in DYX1C1-deficient respiratory cilia

Respiratory cilia isolated from individuals with biallelic *DYX1C1* mutations displayed severe ultrastructural defects (**Fig. 4c**–**f**) resembling the defects observed in mouse *Dyx1c1* mutants (**Fig. 3b**,**c**,**e**). Specifically, both ODA and IDA defects were present in TEM analyses in all ten probands assessed (OP-86 II2, OP-556 II1, UNC1669, UNC1839, UNC1171, UNC158, UNC159, UNC663, UCL-200 II:1 and UCL-200 II:2) (**Fig. 4c** and **Supplementary Table 1**). To further understand the defect at the molecular level, we performed immunofluorescence microscopy of cilia using antibodies targeting components of the axonemal ODA, IDA and N-DRC. Immunofluorescence analysis showed absence of or marked reduction in the levels of the proteins normally present in type 1 and type 2 ODA complexes (DNAH5, DNAH9 and DNAI2; **Fig. 4d**,**e** and **Supplementary Figs. 4**–**6**) as well as for IDA subtype complexes (DNALI1; **Fig. 4f** and **Supplementary Fig. 7**). These findings are similar to cytoplasmic preassembly (DNAAF) defects reported in ciliary axonemes with mutant *DNAAF2* (ref. 20), *DNAAF1* (refs. 21,22) and *DNAAF3* (ref. 23). Notably, we found that the extent of axonemal ODA defects varied among the respiratory cells tested, and, in some cases, the ODA proteins DNAH5 and DNAI2 could be partially detected in the axonemes (**Supplementary Figs. 4** and **6**). Assembly of proximal type 1 ODA complexes (positive and negative for DNAH9) seemed to be better preserved than distally localized type 2 ODA complexes (positive for DNAH5 and DNAH9; **Supplementary Figs. 4**–**6**). To further understand the functional consequences of our observations, we performed nasal brush biopsies in affected individuals (F-648 II1, OP-86 II2, UNC1669, UNC1839, UNC1171, UNC663, UCL-200 II:1 and UCL-200 II:2) and analyzed respiratory cilia beating by high-speed videomicroscopy. Videomicroscopy showed that most respiratory cells had immotile cilia (**Supplementary Videos 12** and **13**); however, cilia were found to beat in some respiratory cells, albeit with reduced frequency (**Supplementary Videos 14** and **15**) relative to control cilia (**Supplementary Video 16**). These variable motility defects in *DYX1C1*-mutant cells are consistent with our previous

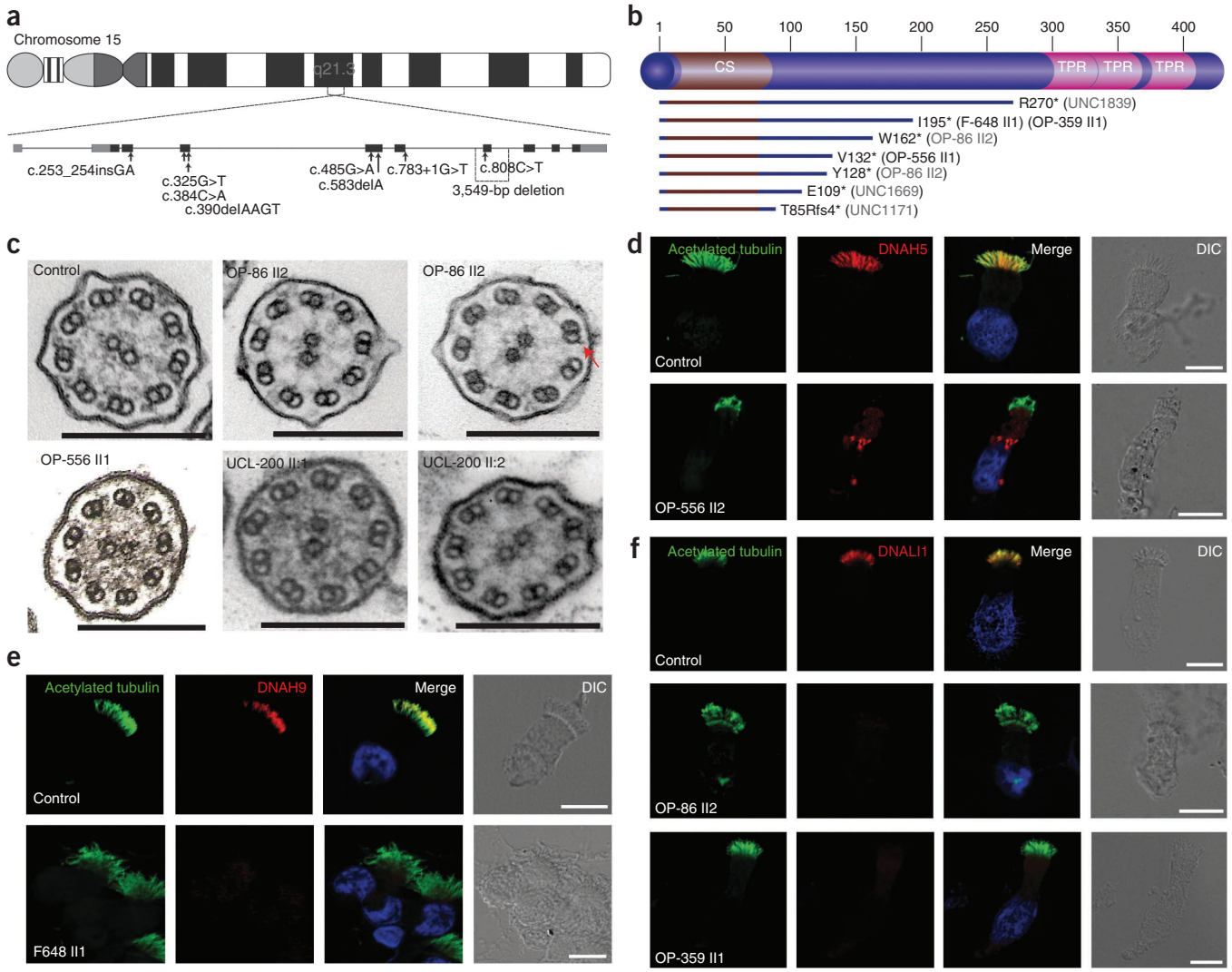

Figure 4 *DYX1C1* mutations in humans cause defective ODA and IDA assembly. (**a**) Schematic of chromosome 15 and the genomic structure of *DYX1C1*. The positions of eight of the identified mutations are indicated by black arrows; the position of the 3.5-kb deletion is indicated by a rectangle. (**b**) Schematic showing the relative positions of seven DYX1C1 nonsense alterations identified in individuals and families with PCD in the *DYX1C1* coding sequence. All alterations are clustered in the middle of the DYX1C1 protein, and each mutation is predicted to introduce a premature stop before the TPR domains at the C terminus of DYX1C1 (CS: p23-like C-terminal CHORD-SGT1 domain). (**c**) TEM images showing defects in ODAs and IDAs in four individuals with PCD with *DYX1C1* mutations compared to a control without PCD. Rarely, ODAs can be seen in the cilia of the affected individual (OP-86 II2, red arrow). Scale bars, 0.2 μm. (**d**) Respiratory epithelial cells from a control individual and PCD OP-556 II2 were double labeled with antibodies directed against acetylated tubulin and DNAH5. Both proteins colocalize along the cilia in cells from the unaffected controls. In contrast, in cells from the affected individual, DNAH5 was absent from or severely reduced in abundance in ciliary axonemes (**Supplementary Fig. 4**). (**e**) Aberrant sublocalization pattern of ODA heavy chain DNAH9 in the cilia of respiratory epithelial cells from a control individual and F648 II1 with PCD. Cells were double labeled with antibodies directed against acetylated tubulin and DNAH9. Acetylated tubulin localizes to the entire length of the cilia, whereas DNAH9 localization is restricted to the distal part of the cilia. In contrast, in *DYX1C1*-mutant cells, DNAH9 was completely absent from ciliary axonemes. (**f**) Respiratory epithelial cells from a control individual and OP-86 II2 and OP-359 II1 with PCD were double labeled with antibodies directed against acetylated tubulin and DNALI1. Both proteins colocalize to the ciliary axonemes in cells from an unaffected control, whereas DNALI1 is absent from ciliary axonemes in *DYX1C1*-mutant cells. In **d**–**f**, nuclei are stained with Hoechst 33342 (blue). Scale bars, 10 μm.

observations of variable degrees of axonemal ODA defects. Notably, only *DNAAF2* mutations in humans have been shown to yield respiratory cells with similarly variable ODA defects and associated IDA abnormalities[20].

Cellular sublocalization and interaction partners of DYX1C1

The phenotypes described above as well as previously reported interactions between exogenously expressed DYX1C1 protein and molecular chaperones suggested to us that DYX1C1 might function as a newly identified cytoplasmic axonemal dynein assembly factor. Consistent with this possibility, we found by immunofluorescence that mouse DYX1C1 protein was located in the cytoplasm of respiratory epithelia (**Fig. 5a**). We confirmed this finding by immunoblot by showing that, similar to DNAAF2, human DYX1C1 was also present in the cytoplasmic protein fraction and was almost undetectable in the axonemal protein fraction of human respiratory cells (**Fig. 5b**). Considering the similarities in phenotype caused by *DYX1C1* and *DNAAF2* mutations with regard to variable ODA defects, we tested for possible

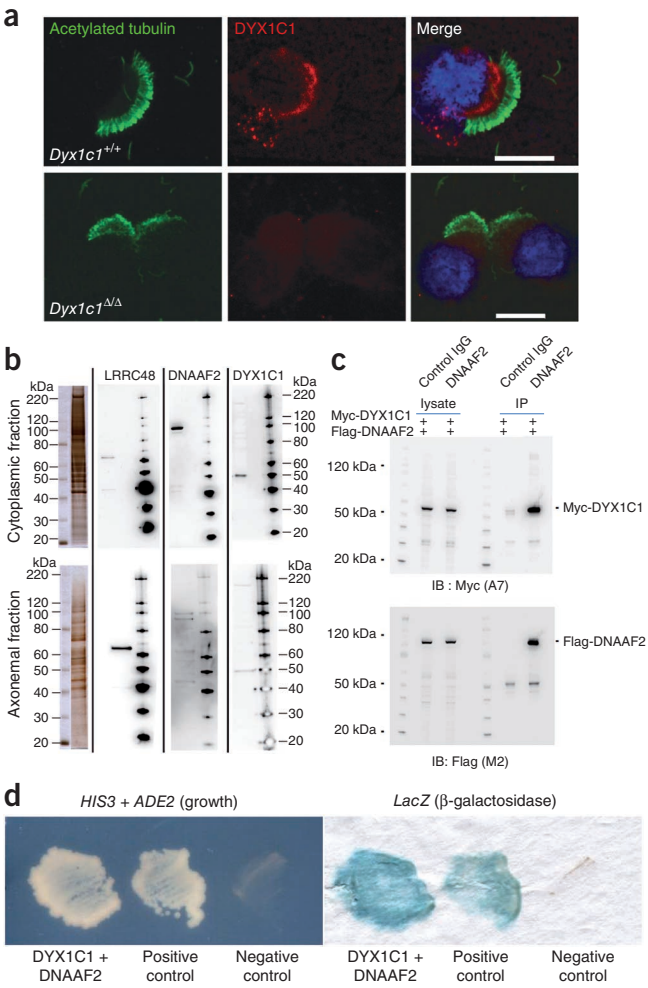

Figure 5 DYX1C1 is localized in the cytoplasm of respiratory epithelial cells and interacts with DNAAF2. (**a**) Immunofluorescence analyses of mouse nasal epithelial cells stained for acetylated tubulin and Dyx1c1. In *Dyx1c1*$^{+/+}$ mice, Dyx1c1 localizes to the cytoplasm of the epithelial cells and partly to the basal bodies but is absent in the cilia. In the mutant, Dyx1c1 is absent from the cytoplasm. Nuclei were stained with Hoechst 33342 (blue). Scale bars, 10 μm. (**b**) Immunoblots performed with different lysate fractions from the cells in **a** (cytoplasmic and axonemal) demonstrate that DYX1C1, as well as DNAAF2, shows a strong signal in the cytoplasmic fraction but is almost absent in the axonemal fraction. LRRC48 was used as an axonemal control. Silver staining of the loaded lysates is shown on the left. (**c**) Lysates from HEK293 cells coexpressing Myc-DYX1C1 and Flag-DNAAF2 were immunoprecipitated with either rabbit control immunoglobulin G (IgG) or rabbit antibody to DNAAF2. Protein blotting (IB) with mouse antibody to Myc demonstrates that Myc-DYX1C1 is efficiently immunoprecipitated by DNAAF2 (top), and protein blotting with mouse antibody to Flag confirms that Flag-DNAAF2 is recovered in the immunoprecipitate (bottom) compared to the control immunoprecipitation. Equal volumes (12 μl) of lysate and immunoprecipitate fractions were loaded on the same gel; lysate fractions represent 1.2% of the total lysate (1-ml volume), and immunoprecipitate fractions represent 6.7% of the lysis volume (33-μl resuspension of a 500-μl volume) Magic Mark protein ladder (M) was used to estimate the molecular weight of Myc-DYX1C1 and Flag-DNAAF2. The observed molecular weights of Myc-DYX1C1 and Flag-DNAAF2 are greater than the expected molecular weights of 48.5 and 91 kDa, respectively, owing to additional sequence from the Myc and Flag epitope tags. (**d**) Yeast two-hybrid assay using GAL4 DNA-binding domain (BD)-tagged DYX1C1 and GAL4 transcription activation domain (AD)-tagged DNAAF2 demonstrates a binary interaction between DYX1C1 and DNAAF2. Binary interactions were identified by yeast growth on medium lacking adenine and histidine to select for *HIS3* and *ADE2* reporter gene activation (left). Interactions were additionally validated by evaluation of *LacZ* reporter gene activation (β-galactosidase colorimetric filter lift assay, right). Binding of BD-DYX1C1 and AD-DNAAF2 was validated using the known interactors BD-USH2A_icd and AD-NINL_isoB as a positive control and BD-USH2A_icd and AD-GAL4 as a negative control.

interactions between these proteins. Using Myc- and Flag-tagged proteins that were coexpressed in HEK293 cells, we found by coimmunoprecipitation that DYX1C1 interacted with DNAAF2 (**Fig. 5c**) but not with the cytoplasmic preassembly factors DNAAF1 and DNAAF3 or with the PCD-associated protein CCDC103 that is localized to both the cytoplasm and axoneme and has a role in dynein-arm attachment (**Supplementary Fig. 8**), as well as with the newly identified dynein-arm assembly protein LRRC6 (data not shown). Furthermore, we demonstrated that DYX1C1 and DNAAF2 interacted directly by yeast two-hybrid assay (**Fig. 5d**). On the basis of these findings, we hypothesize that DYX1C1 represents a new cytoplasmic axonemal dynein assembly factor, possibly acting together with DNAAF2 at an early step in cytoplasmic ODA and IDA assembly.

To categorize the molecular function of DYX1C1 more completely in respiratory tissue, we defined the protein interactome of DYX1C1 in mouse trachea by coimmunoprecipitation and tandem mass spectrometry. We prepared input extracts for coimmunoprecipitation from the trachea tissue of either wild-type or mutant mice and found that these appeared similar in protein composition, as evaluated by Coomassie staining after SDS-PAGE (**Supplementary Fig. 8a**). After coimmunoprecipitation with antibodies to DYX1C1, Coomassie-stained protein bands were apparent in preparations from wild-type extracts but not in those generated from mutant extracts (**Supplementary Fig. 8a**). We cut 14 matched pairs of gel pieces covering the range from approximately 20 to 200 kDa, with many pieces containing multiple bands, from wild-type and mutant coimmunoprecipitations and subjected them to tryptic digestion and tandem mass spectrometry analysis for protein identification. In all, we identified 702 proteins in immunoprecipitates from wild-type trachea and 29 proteins in gel slices from the immunoprecipitates from trachea expressing mutant protein (**Supplementary Table 2**). To determine whether the identified DYX1C1 protein interactome was enriched for particular molecular or biological functions, we used the Database for Annotation, Visualization and Integrated Discovery (DAVID) to determine the presence of enriched Panther Gene Ontology terms in the DYX1C1 interactome and proteins identified in the knockout control. Using a mouse lung proteome as background, we found several molecular functional categories enriched in the DYX1C1 interactome, and several of these were in categories containing molecular chaperones (MF00077: chaperone, $P < 0.001$; BP00062: protein folding, $P < 0.01$; BP00072: protein complex assembly, $P < 0.05$; and MF00078: chaperonin, $P = 0.05$; **Supplementary Table 3**). All four of these chaperone-containing categories were not significantly enriched in the protein set identified in the immunoprecipitates with mutant protein (**Supplementary Table 3**). The DYX1C1 interactome contained a total of 28 proteins in the chaperone or chaperonin category, including 6 of 8 subunits in the T-complex chaperonin complex and multiple heat-shock proteins. We confirmed by coimmunoprecipitation and protein blot analysis the interactions of six chaperones with DYX1C1, including Cct3, Cct4, Cct5, Cct8, Hsp70 and Hsp90 (**Supplementary Fig. 8b**).

DISCUSSION

The protein interactions we found in tracheal tissue with endogenous DYX1C1 are in agreement with the results from a recent study using

exogenously expressed DYX1C1 and neuroblastoma cell lines[45]. Our results provide the first evidence that may link the T complex of chaperones, known primarily for its role in cytoskeletal protein assembly, to the folding and assembly of axonemal dynein complexes. Notably, evidence for a role of Cct proteins in the cytoplasmic assembly of the protein complexes required for motile cilia has been reported for *Tetrahymena*[46]. Although the DYX1C1 mouse interactome defined with tandem mass spectrometry did not include any of the known DNAAF proteins, absence in a tandem mass spectrometry screen does not necessarily mean absence of interaction and highlights the importance of screening for potential interactors by several means.

This study is the first to our knowledge to show the effects of DYX1C1 deficiency in humans, mice and zebrafish. The phenotypes in all species are consistent in showing a selective defect in motile cilia, reflecting deficient dynein-arm transport or assembly. Furthermore, because the human subjects in this study with mutations in *DYX1C1* showed no evidence of dyslexia, we propose that the loss of DYX1C1 function might not be a highly penetrant cause of dyslexia. In conclusion, on the basis of the pattern of cilia defects observed, its cellular localization, a protein interactome enriched for chaperones and genetic-physical interaction with DNAAF2, we propose that DYX1C1 represents a new axonemal dynein assembly factor (DNAAF4).

URLs. ZFIN Direct Data Submission, http://zfin.org/; UK10K group, http://uk10k.org.uk/; complex congenital heart disease (CCHD) database, http://www.informatics.jax.org/javawi2/servlet/WIFetch?page=alleleDetail&id=MGI:5311375; Mascot Distiller program, http://www.matrixscience.com/home.html; Global Proteome Machine, http://www.thegpm.org/lists/index.html; DAVID Bioinformatics Resources 6.7, http://david.abcc.ncifcrf.gov/.

METHODS

Methods and any associated references are available in the online version of the paper.

Accession codes. All cDNA clones were confirmed by sequence analysis and matched the following gene accessions: NM_130810.3 (*DYX1C1*), NM_178452.4 (*DNAAF1*), BC016843 (*DNAAF3*), NM_213607.2 (*CCDC103*) and NM_018139.2 (*DNAAF2*).

Note: Any Supplementary Information and Source Data files are available in the online version of the paper.

ACKNOWLEDGMENTS

We thank the individuals with PCD and their families for participating in this study, the German patient support group Kartagener Syndrom und Primaere Ciliaere Dyskinesie and the US PCD foundation. We thank S. King (University of Connecticut Health Center) for providing antibodies and for helpful discussions. This work was funded by the Deutsche Forschungsgemeinschaft (DFG Om 6/4), by the Interdisziplinaeres Zentrum für Klinische Forschung (IZKF) Münster (H. Omran), by the European Community's Seventh Framework Programme FP7/2009, under grant agreement 241955, SYSCILIA (R.R. and H. Omran), and BESTCILIA, under grant agreement 305404 (H. Omran), by the Netherlands Organization for Scientific Research (NWO; Vidi-91786396 and Vici-016.130.664) (R.R.) and by grants from the US National Institutes of Health (NIH; R01 HD055655, R01 MH056524 and P01 HD057853 (J.J.L.): research grant 5 U54 HL096458-06 (M.R.K., M.W.L., J.L.C. and M.A.Z.); NHLBI grant 5 R01HL071798 (M.R.K. and M.A.Z.); National Institute of Child Health and Human Development (NICHD) grant 2 R01HD048584 (C.E.S., J.V.T., S.C. and R.D.B.); NIH grant U01HL098180 (C.W.L.); and American Heart Association fellowship (Y.L.). The work was also supported by Newlife Foundation grant 10/11/15 (H.M.M.) and Action Medical Research grant RTF1411 (M.S.). UK10K was funded by the Wellcome Trust (award WT091310). This work was supported in part by US NIH grant UL1 TR000083 from the National Center for Advancing Translational Sciences (NCATS).

AUTHOR CONTRIBUTIONS

J.J.L. and H. Omran designed the study. N.T.L., C.J., H. Olbrich, R.H., G.W.D., P.P., M.A., D.A.M., S.J.F.L., R.R., K.B. and J.R. performed experiments with human *DYX1C1* and analyzed the data. G.K., C.W., J.R., M.G., M.J. and H. Omran provided clinical data on OP cases. M.A.Z., L.C.M., A.J.S., J.L.C., M.W.L., W.E.W. and M.R.K. performed mutational analyses and provided clinical data from UNC cases. J.S.L. performed clinical ascertainment of UCL cases. A.O., M.S. and H.M.M. performed mutation analysis of UCL cases. V.P. developed the deletion algorithm for UCL cases. UK10K performed exome sequencing of UK samples. A.T., B.S., M.C., N.T.L., D.S., P.P. and M.A. performed experiments with mouse *Dyx1c1* and analyzed the data. C.W.L., R.F., Y.L., K.L., N.K., X.L., G.G. and K.T. performed experiments with the mouse *Sharpei* mutant and analyzed the data. C.E.S., J.V.T., S.C. and R.D.B. performed the zebrafish experiments and analyses. D.A.M., S.J.F.L. and R.R. contributed to the yeast two-hybrid experiments.

COMPETING FINANCIAL INTERETS

The authors declare no competing financial interests.

1. Fliegauf, M., Benzing, T. & Omran, H. When cilia go bad: cilia defects and ciliopathies. *Nat. Rev. Mol. Cell Biol.* **8**, 880–893 (2007).
2. Kennedy, M.P. *et al.* Congenital heart disease and other heterotaxic defects in a large cohort of patients with primary ciliary dyskinesia. *Circulation* **115**, 2814–2821 (2007).
3. Ibañez-Tallon, I. *et al.* Dysfunction of axonemal dynein heavy chain Mdnah5 inhibits ependymal flow and reveals a novel mechanism for hydrocephalus formation. *Hum. Mol. Genet.* **13**, 2133–2141 (2004).
4. Olbrich, H. *et al.* Mutations in *DNAH5* cause primary ciliary dyskinesia and randomization of left-right asymmetry. *Nat. Genet.* **30**, 143–144 (2002).
5. Pennarun, G. *et al.* Loss-of-function mutations in a human gene related to *Chlamydomonas reinhardtii* dynein IC78 result in primary ciliary dyskinesia. *Am. J. Hum. Genet.* **65**, 1508–1519 (1999).
6. Panizzi, J.R. *et al.* *CCDC103* mutations cause primary ciliary dyskinesia by disrupting assembly of ciliary dynein arms. *Nat. Genet.* **44**, 714–719 (2012).
7. Loges, N.T. *et al.* *DNAI2* mutations cause primary ciliary dyskinesia with defects in the outer dynein arm. *Am. J. Hum. Genet.* **83**, 547–558 (2008).
8. Mazor, M. *et al.* Primary ciliary dyskinesia caused by homozygous mutation in *DNAL1*, encoding dynein light chain 1. *Am. J. Hum. Genet.* **88**, 599–607 (2011).
9. Duriez, B. *et al.* A common variant in combination with a nonsense mutation in a member of the thioredoxin family causes primary ciliary dyskinesia. *Proc. Natl. Acad. Sci. USA* **104**, 3336–3341 (2007).
10. Bartoloni, L. *et al.* Mutations in the *DNAH11* (axonemal heavy chain dynein type 11) gene cause one form of *situs inversus totalis* and most likely primary ciliary dyskinesia. *Proc. Natl. Acad. Sci. USA* **99**, 10282–10286 (2002).
11. Schwabe, G.C. *et al.* Primary ciliary dyskinesia associated with normal axoneme ultrastructure is caused by *DNAH11* mutations. *Hum. Mutat.* **29**, 289–298 (2008).
12. Knowles, M.R. *et al.* Mutations of *DNAH11* in patients with primary ciliary dyskinesia with normal ciliary ultrastructure. *Thorax* **67**, 433–441 (2012).
13. Merveille, A.C. *et al.* *CCDC39* is required for assembly of inner dynein arms and the dynein regulatory complex and for normal ciliary motility in humans and dogs. *Nat. Genet.* **43**, 72–78 (2011).
14. Becker-Heck, A. *et al.* The coiled-coil domain containing protein *CCDC40* is essential for motile cilia function and left-right axis formation. *Nat. Genet.* **43**, 79–84 (2011).
15. Castleman, V.H. *et al.* Mutations in radial spoke head protein genes *RSPH9* and *RSPH4A* cause primary ciliary dyskinesia with central-microtubular-pair abnormalities. *Am. J. Hum. Genet.* **84**, 197–209 (2009).
16. Ziętkiewicz, E. *et al.* Mutations in radial spoke head genes and ultrastructural cilia defects in East-European cohort of primary ciliary dyskinesia patients. *PLoS ONE* **7**, e33667 (2012).
17. Olbrich, H. *et al.* Recessive *HYDIN* mutations cause primary ciliary dyskinesia without randomization of left-right body asymmetry. *Am. J. Hum. Genet.* **91**, 672–684 (2012).
18. Budny, B. *et al.* A novel X-linked recessive mental retardation syndrome comprising macrocephaly and ciliary dysfunction is allelic to oral-facial-digital type I syndrome. *Hum. Genet.* **120**, 171–178 (2006).
19. Moore, A. *et al.* *RPGR* is mutated in patients with a complex X linked phenotype combining primary ciliary dyskinesia and retinitis pigmentosa. *J. Med. Genet.* **43**, 326–333 (2006).
20. Omran, H. *et al.* Ktu/PF13 is required for cytoplasmic pre-assembly of axonemal dyneins. *Nature* **456**, 611–616 (2008).
21. Loges, N.T. *et al.* Deletions and point mutations of *LRRC50* cause primary ciliary dyskinesia due to dynein arm defects. *Am. J. Hum. Genet.* **85**, 883–889 (2009).

22. Duquesnoy, P. *et al.* Loss-of-function mutations in the human ortholog of *Chlamydomonas reinhardtii ODA7* disrupt dynein arm assembly and cause primary ciliary dyskinesia. *Am. J. Hum. Genet.* **85**, 890–896 (2009).
23. Mitchison, H.M. *et al.* Mutations in axonemal dynein assembly factor *DNAAF3* cause primary ciliary dyskinesia. *Nat. Genet.* **44**, 381–389 (2012).
24. Kott, E. *et al.* Loss-of-function mutations in *LRRC6*, a gene essential for proper axonemal assembly of inner and outer dynein arms, cause primary ciliary dyskinesia. *Am. J. Hum. Genet.* **91**, 958–964 (2012).
25. Taipale, M. *et al.* A candidate gene for developmental dyslexia encodes a nuclear tetratricopeptide repeat domain protein dynamically regulated in brain. *Proc. Natl. Acad. Sci. USA* **100**, 11553–11558 (2003).
26. Bates, T.C. *et al.* Dyslexia and *DYX1C1*: deficits in reading and spelling associated with a missense mutation. *Mol. Psychiatry* **15**, 1190–1196 (2010).
27. Marino, C. *et al.* Association of short-term memory with a variant within *DYX1C1* in developmental dyslexia. *Genes Brain Behav.* **6**, 640–646 (2007).
28. Wigg, K.G. *et al.* Support for *EKN1* as the susceptibility locus for dyslexia on 15q21. *Mol. Psychiatry* **9**, 1111–1121 (2004).
29. Meng, H. *et al.* TDT-association analysis of *EKN1* and dyslexia in a Colorado twin cohort. *Hum. Genet.* **118**, 87–90 (2005).
30. Marino, C. *et al.* A family-based association study does not support *DYX1C1* on 15q21.3 as a candidate gene in developmental dyslexia. *Eur. J. Hum. Genet.* **13**, 491–499 (2005).
31. Scerri, T.S. *et al.* Putative functional alleles of *DYX1C1* are not associated with dyslexia susceptibility in a large sample of sibling pairs from the UK. *J. Med. Genet.* **41**, 853–857 (2004).
32. Chen, Y. *et al.* A novel role for DYX1C1, a chaperone protein for both Hsp70 and Hsp90, in breast cancer. *J. Cancer Res. Clin. Oncol.* **135**, 1265–1276 (2009).
33. Hatakeyama, S., Matsumoto, M., Yada, M. & Nakayama, K.I. Interaction of U-box-type ubiquitin-protein ligases (E3s) with molecular chaperones. *Genes Cells* **9**, 533–548 (2004).
34. Massinen, S. *et al.* Functional interaction of DYX1C1 with estrogen receptors suggests involvement of hormonal pathways in dyslexia. *Hum. Mol. Genet.* **18**, 2802–2812 (2009).
35. Wang, Y. *et al.* DYX1C1 functions in neuronal migration in developing neocortex. *Neuroscience* **143**, 515–522 (2006).
36. Rosen, G.D. *et al.* Disruption of neuronal migration by RNAi of *Dyx1c1* results in neocortical and hippocampal malformations. *Cereb. Cortex* **17**, 2562–2572 (2007).
37. Hoh, R.A. *et al.* Transcriptional program of ciliated epithelial cells reveals new cilium and centrosome components and links to human disease. *PLoS ONE* **7**, e52166 (2012).
38. Ivliev, A.E. *et al.* Exploring the transcriptome of ciliated cells using *in silico* dissection of human tissues. *PLoS ONE* **7**, e35618 (2012).
39. Vogel, P. *et al.* Congenital hydrocephalus in genetically engineered mice. *Vet. Pathol.* **49**, 166–181 (2012).
40. Okada, Y. *et al.* Abnormal nodal flow precedes *situs inversus* in *iv* and *inv* mice. *Mol. Cell* **4**, 459–468 (1999).
41. Tan, S.Y. *et al.* Heterotaxy and complex structural heart defects in a mutant mouse model of primary ciliary dyskinesia. *J. Clin. Invest.* **117**, 3742–3752 (2007).
42. Chandrasekar, G. *et al.* The zebrafish orthologue of the dyslexia candidate gene *DYX1C1* is essential for cilia growth and function. *PLoS ONE* **8**, e63123 (2013).
43. Ahmad, N. *et al.* A southpaw joins the roster: the role of the zebrafish nodal-related gene *southpaw* in cardiac LR asymmetry. *Trends Cardiovasc. Med.* **14**, 43–49 (2004).
44. Plagnol, V. *et al.* A robust model for read count data in exome sequencing experiments and implications for copy number variant calling. *Bioinformatics* **28**, 2747–2754 (2012).
45. Tammimies, K. *et al.* Molecular networks of *DYX1C1* gene show connection to neuronal migration genes and cytoskeletal proteins. *Biol. Psychiatry* **73**, 583–590 (2013).
46. Seixas, C. *et al.* CCTα and CCTδ chaperonin subunits are essential and required for cilia assembly and maintenance in *Tetrahymena*. *PLoS ONE* **5**, e10704 (2010).

ONLINE METHODS

Gene targeting and genotyping of *Dyx1c1*$^{\Delta/\Delta}$ mice. Mice carrying the *loxP*–exon 2–4–*loxP* conditional allele of *Dyx1c1* (*Dyx1c1*$^{flox2-4}$) were generated by the University of Connecticut Health Center Gene Targeting and Transgenic Facility. Embryonic stem cells harboring a *loxP*-flanked allele of exons 2–4 of *Dyx1c1* were produced by electroporating mouse embryonic stem (ES) cells (129S6) with a targeting construct designed to replace exons 2–4 and flanking intronic sequence through homologous recombination. We screened 96 ES cell clones by PCR for correctly targeted colonies. A single positive colony was expanded and used for embryo reaggregation to produce five chimeric mice. Three of these mice were shown to transmit the targeted allele through the germ line to offspring in a cross with C57BL/6J mice. The *PGK-Neo* cassette in the targeting construct was then removed by crossing these mice with *129S4/SvJaeSor-Gt(ROSA)26Sor*$^{tm1(FLP1)Dym}$*/J* mice (The Jackson Laboratory). These offspring were used to generate a colony of *Dyx1c1*$^{flox2-4/flox2-4}$ mice. To generate *Dyx1c1*$^{del2-4/del2-4}$ (*Dyx1c1*$^{\Delta/\Delta}$) mice with a deletion of exons 2–4, we crossed *Dyx1c1*$^{flox2-4/flox2-4}$ mice with hypoxanthine-guanine phosphoribosyltransferase (*Hprt*)-*cre* mice, *C57B6/6-Hprtt*$^{m1(cre)Mnn}$*/J* (University of Connecticut Health Center). Genotyping was subsequently performed by PCR using two pairs of primers (**Fig. 1a** and **Supplementary Table 4**). Animal procedures were performed under protocols approved by the Institutional Animal Care and Use Committee of the University of Connecticut and conform to US NIH guidelines.

Whole-mount *in situ* hybridization of *Dyx1c1* mouse embryos. Sense and antisense probes for *Dyx1c1* were generated from a 554-bp pCRII-TOPO construct (nucleotides 1098–1651; RefSeq NM_026314.3, *Mus musculus Dyx1c1* transcript variant 1) produced by TOPO TA cloning (Invitrogen) after amplification from cDNA. Probes were synthesized with digoxigenin NTPs (Roche) after template linearization with HindIII (antisense) or NotI (sense) before RNA synthesis with T7 or SP6 RNA polymerase, respectively. For whole-mount *in situ* hybridization, staged embryos were fixed overnight at 4 °C in 4% paraformaldehyde in 1× PBS. Whole-mount *in situ* hybridization was then performed according to standard procedures with minor modifications[47]. Stained samples were transferred into 80% glycerol, and images were captured using a Scion CFW-1310C color digital camera mounted on an Axioskop2 plus microscope (Zeiss) and Image-Pro Express.

Immunohistochemistry of mouse tissue. Mice were perfused transcardially with 0.9% saline followed by 4% paraformaldehyde (Electron Microscopy Science) in 1× PBS. Brains were removed, fixed overnight in the same fixative at 4 °C and washed in 1× PBS three times for 40 min the next day before cutting into 50-μm sections with a vibratome (VT-1000S, Leica). Nuclei were counterstained with Hoechst 33342 (2 μg/ml in PBS; Sigma). Stained sections were washed for 10 min in PBS, coverslips were applied using Prolong Gold Antifade (Invitrogen), and images were acquired on a Carl Zeiss Axiovert 200M inverted microscope with an ApoTome attachment and Axiovision 4.6 software (Carl Zeiss). Whole mounts of the entire lateral wall of the lateral ventricles were prepared as described previously[48], fixed overnight in 4% paraformaldehyde in PBS at 4 °C and washed in 1× PBS three times for 40 min the next day. They were then permeabilized with 0.1% Triton X-100 (Sigma) in PBS for 10 min, blocked in 10% goat serum (Invitrogen) in PBS and 0.1% Triton X-100 for 1 h, and incubated with the following primary antibodies: mouse antibody to acetylated tubulin (1:500 dilution; Sigma, T6793), rabbit antibody to β-catenin (1:100 dilution; Cell Signaling Technology, 9562) and mouse antibody to γ-tubulin (1:500 dilution; Sigma, T6557). After washing three times in PBS, tissues were incubated with appropriate Alexa Fluor dye–conjugated secondary antibodies (Goat Anti-Rabbit 488 (A11008), Goat Anti-Mouse 488 (A11001), Goat Anti-Rabbit 568 (A11011) and Goat Anti-Mouse 568 (A11031), Invitrogen) at a dilution of 1:400 for 1 h. Tissues were washed in PBS and incubated for 5 min in 2 μg/ml Hoechst 33342 (Sigma) for counterstaining of nuclei. Secondary antibodies alone were used as a control. Whole mounts were placed onto depressed glass slides, and cover slips with CoverWell imaging chambers (Grace Bio-Labs) were applied. Samples were imaged either on a Carl Zeiss Axiovert 200M inverted microscope with an ApoTome attachment and Axiovision 4.6 software (Carl Zeiss) or on a Leica TCS SP2 confocal laser scanning microscope.

Immunofluorescence of dissociated mouse nasal epithelial cells. Nasal epithelial cells were harvested from mouse septa by acute dissociation on a 4-well slide in 1:1 PBS/HBSS. Slides were dried to let the cells adhere to the wells, and cells were immediately fixed with 4% paraformaldehyde for 2 min at room temperature. Cells were then washed twice with 1× PBS for 2 min for each wash. Blocking buffer (10% goat serum and 0.1% Triton X-100 in 1× PBS) was added for 15 min at room temperature. Slides were incubated with rabbit polyclonal antibody to DYX1C1 (Sigma, SAB4200128) at a 1:500 dilution and mouse monoclonal antibody to acetylated tubulin (Sigma, T7451) at a 1:1,000 dilution in the same blocking buffer for 30 min at room temperature. After three washes with 1× PBS for 5 min each, slides were incubated with Alexa Fluor 488–conjugated goat antibody to rabbit (Invitrogen, A11034; 1:5,000 dilution) and Alexa Fluor 568–conjugated goat antibody to mouse (Invitrogen, A11031; 1:1,000 dilution) for 20 min at room temperature. Slides were washed twice with 1× PBS for 5 min each, and nuclear stain Hoechst 33342 (Invitrogen, H3570) at a 1:2,500 dilution was added for 15 min at room temperature. Slides were dried, and cover slips were applied with Prolong Gold Antifade (Invitrogen, P36930). Cells were imaged on a Leica TCS Sp2 laser scanning microscope.

TEM. To collect brains, mice (12 d old) were perfused transcardially with 0.9% saline followed by 2% paraformaldehyde/2.5% glutaraldehyde in 0.1 mM phosphate buffer. Brain samples were further fixed by immersion overnight in 2% paraformaldehyde/2.5% glutaraldehyde in 0.1 mM phosphate buffer and were washed in phosphate buffer three times for 40 min per wash. Sections were postfixed with 2% OsO_4 in 0.1 mM phosphate buffer for 1.5 h and were dehydrated through a graded ethanol series. After dehydration, tissues were washed twice in acetone and embedded in epoxy resin in capped inverted Beem capsules. Thin sections were cut with a diamond knife, placed onto Formvar-coated slot grids and heavy metal stained with uranyl acetate and lead citrate. Trachea tissues were directly dissected without perfusion and were fixed by immersion overnight in 2% paraformaldehyde/2.5% glutaraldehyde in 0.12 mM phosphate buffer. They were washed in phosphate buffer three times (60 min in total), postfixed in 1% OsO_4 and 0.8% potassium ferricyanide in 0.12 M phosphate buffer for 1 h, dehydrated through a graded ethanol series, rinsed twice in acetone and embedded in epoxy resin. Thin sections were cut with a diamond knife, placed on copper grids and heavy metal stained with ethanolic uranyl acetate and Sato's lead citrate. Electron micrographs were captured using an FEI Tecnai 12 Biotwin TEM equipped with a side-mounted AMT XR-40 CCD camera and Epson Expression 1680 flatbed scanners.

Scanning electron microscopy. Wild-type and mutant mouse embryos (E7.5) were collected and fixed in 1.5% paraformaldehyde/1.5% glutaraldehyde in 0.10 M sodium cacodylate containing 0.05 M NaCl overnight at 4 °C. Samples were postfixed with 2% OsO_4 in the same buffer overnight and were dehydrated using a graded ethanol series. Specimens were dried in a Polaron E3000 Critical-Point Dryer and mounted onto aluminum specimen mounts (Ted Pella) using carbon tape and silver paint (Ernest F. Fullam). Each mount was sputter coated with gold palladium (60% gold, 40% palladium) using a Polaron E5100 Sputter Coater. Samples were examined and photographed using a LEO DSM982 field emission scanning electron microscope.

Protein blots of brain, lung and trachea lysates. Wild-type and mutant mouse brains and lungs were collected and lysed in RIPA Buffer (Sigma) supplemented with 1× Protease Inhibitor Cocktail (Sigma). For tracheal and lung preparation, tissues were dissected and carefully separated from the surrounding tissues. Samples were homogenized using a tissue homogenizer and cleared by centrifugation at 10,000*g* for 10 min. Proteins were separated on 10% SDS-PAGE minigels and then transferred to Immobilon (Millipore) membrane for protein blotting. For detecting DYX1C1 protein, the antibody to N-terminal DYX1C1 (Sigma, SAB4200128) was used at a dilution of 1:200; antibody to GAPDH (Sigma, G8795) was used at a 1:1,500 dilution as a loading control. LI-COR Odyssey infrared secondary antibodies (goat antibody to mouse 680 (926-32220), goat antibody to mouse 800 (926-32210) goat antibody to mouse 680 (926-32221) and goat antibody to mouse 800 (926-32211)) were used at dilutions of 1:10,000. All blots were imaged and analyzed using a LI-COR Odyssey Scanner and Software.

doi:10.1038/ng.2707

Immunoprecipitation. Immunoprecipitation assays were performed using the Dynabeads Protein G Immunoprecipitation kit (Invitrogen). Briefly, Dynabeads were resuspended in the vial and separated on a magnet from solution. Antibody to N-terminal DYX1C1 (5 μg) was diluted in 200 μl of Washing and Binding Solution and incubated with rotation for 60 min at room temperature. Bead-antibody complexes were separated on the magnet, washed by gentle pipetting and separated. Protein lysates from wild-type and mutant mouse brains were incubated with the bead-antibody complexes overnight at 4 °C. Bead-antibody-antigen complexes were then washed using the washing solution three times. Complexes were then incubated with elution buffer for 10–15 min to dissociate them. Beads were separated on a magnet, and supernatant containing the proteins was separated by SDS-PAGE and analyzed by protein blotting using monoclonal antibody to DNAI2 (Abnova, M01, clone 1C8; 1:500 dilution), antibody to Hsp70 (BD Biosciences, 610607; 1:1,000 dilution), antibody to Hsp90 (BD Biosciences, 610418; 1:1,000 dilution), antibody to CCT4 (Aviva Systems Biology, ARP34271_P050; 1:500 dilution), antibody to CCT3 (Proteintech, 10571-1-AP; 1:500 dilution), antibody to CCT5 (Proteintech, 11603-1-AP; 1:500 dilution), antibody to CCT8 (Proteintech, 12263-1-AP; 1:500 dilution) and monoclonal antibody to IC74 (a gift from S. King; 1:750 dilution). Rabbit IgG was used as a control.

Basic peptide identification by tandem mass spectrometry. After separation by SDS-PAGE, proteins were stained with Coomassie dye. Fourteen gel pieces were excised from the gels that contained bands in the immunoprecipitates with wild-type Dyx1c1 or were adjacent to these bands in the lane containing immunoprecipitates with mutant Dyx1c1. Bands were in-gel digested with trypsin, and resulting peptides were analyzed using liquid chromatography tandem mass spectrometry on a Thermo Scientific LTQ-Orbitrap XL mass spectrometer equipped with Waters nanaoACQUITY ultra-high-pressure liquid chromatographs (UPLCs) for peptide separation. The liquid chromatography tandem mass spectrometry data were searched with an in-house Mascot algorithm for uninterpreted tandem mass spectrometry spectra after using the Mascot Distiller program to generate Mascot compatible files. Charge states of +2 and +3 were preferentially located with a signal-to-noise ratio of 1.2 or greater, and a peak list was generated for database searching. NCBInr, a mouse-specific database (in FASTA format), was used for searching.

Tandem mass spectrometry and gene ontology enrichment analysis. Raw tandem mass spectrometry peptide sequencing results for the wild-type and control analyses obtained from the Yale W.M. Keck Foundation Proteomics Resource were stringently filtered to ensure a low false positive protein identification rate. Specifically, proteins were considered identified only if they contained two or more unique peptides with expectation values of ≤0.01 (**Supplementary Table 3**). Resulting unique protein GI accession numbers for the wild-type and controls were separately used as inputs for the DAVID bioinformatics resource with the mouse proteome selected as the background[49,50]. To detect enrichment in gene ontology terms associated with the input proteins, the PANTHER biological process and PANTHER molecular function annotations were selected, and functional annotation charts were generated (**Supplementary Table 3**). To further account for high-abundance proteins commonly observed in tandem mass spectrometry analyses, a list of 1,000 mouse protein Swiss-Prot accession numbers was obtained from the Global Proteome Machine web site and was used as an alternate background in the DAVID gene ontology analysis of DYX1C1 interactors.

Videomicroscopy of ependymal flow and cilia in mice. P6–P10 wild-type and mutant mice were deeply anesthetized with isoflurane and were then decapitated. Brains were rapidly removed and immersed in ice-cold oxygenated (95% O_2 and 5% CO_2) dissection buffer containing 83 mM NaCl, 2.5 mM KCl, 1 mM NaH_2PO_4, 26.2 mM $NaHCO_3$, 22 mM glucose, 72 mM sucrose, 0.5 mM $CaCl_2$ and 3.3 mM $MgCl_2$. The lateral wall of the lateral ventricle was dissected using a fine scalpel and forceps and was immediately observed in a chamber containing buffer at 37 °C. For visualization of flow, a small amount of India ink was placed on the surface of the lateral wall of the dissected ventricle. Movement of India ink was observed and recorded using infrared DIC microscopy (E600FN, Nikon) and a CCD camera (QICAM, QImaging, 120 frames per second (fps)). For direct observation of cilia movement, mouse brains were harvested as above, and coronal slices (400 μm) were cut using a vibratome (Leica, VT1200S). Slices from the third ventricle through the fourth ventricle were visualized using infrared DIC and a CCD camera. Images were analyzed with ImageJ software (NIH).

Morpholino injection of zebrafish embryos. Morpholino antisense oligonucleotides (Gene Tools) were maintained in 1 mM stock solutions in water at 4 °C. The translation-blocking *dyx1c1* morpholino (**Supplementary Table 5**) spanned the start codon and produced phenotypes at 2 ng per embryo. A second, splice-blocking *dyx1c1* morpholino (**Supplementary Table 5**) spanned the splice site between exon 2 and the following intron and produced phenotypes at 4–6 ng per embryo. Phenotypes produced by both morpholinos were similar, demonstrating the specificity of the morpholinos for *dyx1c1*. Morpholinos were mixed with 5 mg/ml phenol red and injected into embryos at the one- to four-cell stage as described[51]. Brightfield video microscopy of Kupffer's vesicles was performed on an inverted Leica SP5 spectral microscope. Live embryos were mounted in 2% low-melt agarose in glass-bottom tissue culture dishes and were illuminated with light at a wavelength of 561 nm. Recordings were captured at 170 fps using a 63× glycerin immersion objective.

RNA probes and whole-mount *in situ* hybridization of zebrafish embryos. DIG-labeled RNA probes were transcribed from linearized DNA templates and used in RNA *in situ* hybridization with standard methods. Antisense probes included *cardiac myosin light chain* (*cmlc2*; *myl7*-ZFIN)[52], *forkhead 2* (*fkd2*; *foxa3*-ZFIN)[53], *preproinsulin* (*ins*)[54] and *southpaw* (*spaw*)[43].

Microscopy of zebrafish embryos. Images of live zebrafish embryos were taken using the ProgressC14 digital camera (Jenoptik) mounted on a Leica MZFL III microscope. Embryos processed for *in situ* hybridization analysis were mounted in modified GMM[55] (100 ml of Canada Balsam (Sigma, C-1795) and 10 ml of methylsalicylate (Sigma, M0387-100G)), visualized using a Leica DMRA microscope at 10× magnification and photographed with the ProgressC14 digital camera.

Mutational analysis of individuals with PCD. Signed and informed consent was obtained from individuals fulfilling diagnostic criteria of PCD[56] and family members using protocols approved by the Institutional Ethics Review Board at the University of Münster and the University College London Hospital NHS Trust. Genomic DNA was isolated using standard methods directly from blood samples or from lymphocyte cultures after Epstein-Barr virus (EBV)-mediated transformation. Exome analysis of family UCL200 was performed as part of the UK10K Project, as previously described[15]. Amplification of ten genomic fragments comprising all ten exons of *DYX1C1* was performed for each exon and subject in a volume of 50 μl containing 30 ng of DNA, 50 pmol of each primer, 2 mM dNTPs and 1.0 U GoTaq DNA polymerase (Promega). PCR amplifications were carried out by means of an initial denaturation step at 94 °C for 3 min and 33 cycles at 94 °C for 30 s, 58–60 °C for 30 s and 72 °C for 70 s, with a final extension step at 72 °C for 10 min. PCR products were verified by agarose gel electrophoresis, purified using ExoSAP-IT (Affymetrix) and sequenced bidirectionally using the BigDye Terminator v3.1 Cycle Sequencing kit (Applied Biosystems). Samples were separated and analyzed on an Applied Biosystems 3730xl DNA Analyzer. Sequence data were evaluated using CodonCode software.

TEM of human respiratory cilia. TEM of human respiratory cilia was performed as previously described[17].

High-speed video microscopy analysis of ciliary beat in human cilia. Ciliary beat was assessed with the SAVA system[57]. Respiratory epithelial cells were viewed with an Olympus IMT-2 microscope (40 phase contrast objective) equipped with a Redlake ES-310Turbo monochrome high-speed video camera set at 125 fps. Ciliary beating patterns were evaluated on slow-motion playbacks.

Immunofluorescence of human respiratory epithelium. Respiratory epithelial cells were obtained by nasal brush biopsy (Engelbrecht Medicine and

Laboratory Technology) and suspended in cell culture medium. Samples were spread onto glass slides, air dried and stored at −80 °C until use. Cells were treated with 4% paraformaldehyde, 0.2% Triton X-100 and 1% skim milk before incubation with primary antibody (for 2–3 h at room temperature or overnight at 4 °C) and secondary antibody (for 25 min at room temperature). Appropriate controls were performed omitting the primary antibodies. Mouse monoclonal antibody to DNAI2 (1:200 dilution; H00064446-M01 (clone1C8)) was obtained from Abnova. Mouse monoclonal antibody to acetylated tubulin (1:10,000 dilution; T7451-200UL) and rabbit polyclonal antibody to CCDC39 (1:300 dilution; HPA035364) were obtained from Sigma. Rabbit polyclonal antibodies to DNAH5 and DNALI1 were generated as reported[58,59]. Highly cross-adsorbed secondary antibodies, including Alexa Fluor 488–conjugated goat antibody to mouse (1:1,000 dilution; A11029) and Alexa Fluor 546–conjugated goat antibody to rabbit (1:1,000 dilution; A11035), were from Molecular Probes (Invitrogen). DNA was stained with Hoechst 33342 (1:1,000 dilution; 14533-100MG, Sigma) or DAPI (1:1,000 dilution; 32670-25MG-F, Sigma). Immunofluorescence images were taken with a Zeiss Apotome Axiovert 200 microscope and processed with AxioVision 4.8 and Adobe Creative Suite 4.

cDNA cloning. The following clones were purchased from Origene: *DYX1C1* (SC313387), *DNAAF3* (SC126165) and *CCDC103* (RC208345). cDNA clones for *DNAAF2* and *DNAAF1* were amplified by two-step (nested) PCR from human bronchial epithelial cell cDNA (3214, ScienCell; **Supplementary Table 6**) for Gateway cloning. All PCR products were amplified using KOD polymerase according to the manufacturer's directions, recombined with the pDONR201 Gateway vector via BP Clonase II reaction and subcloned into Gateway entry vectors encoding Myc and 3× Flag epitope tags via LR Clonase reaction.

Preparation of human respiratory cell lysates. Human respiratory cells were obtained either by brushing or cell culture (spheroids)[60]. Cells were incubated in 800–1,000 µl of NP-40 or RIPA lysis buffer containing protease inhibitor cocktail (P8340, Sigma-Aldrich) on ice for 30 min and were occasionally vortexed. Lysates were spun at 20,817*g* at 4 °C for 10 min. Supernatants were moved to a new tube (cytoplasmic fraction). Pellets were resuspended in 100–150 µl of modified Reeds high-salt extraction buffer[61] (30 mM HEPES, pH 7.4, 5 mM $MgSO_4$, 0.1 mM EDTA, 625 mM NaCl, 2 mM DTT, 70 mM β-mercaptoethanol and 0.1% Triton X-100) containing protease inhibitor cocktail (P8340, Sigma-Aldrich) and incubated on ice for 30–60 min with frequent vortexing. Lysates were spun down at 20,817*g* at 4 °C for 10 min. Supernatants were moved to a new tube (axonemal fraction). Lysates were visualized by silver staining using the ProteoSilver silver staining kit (PROTSIL1-1KT, Sigma-Aldrich) and stored at −20 °C or −80 °C until use. Using this method, we obtained two protein fractions, the first enriched for cytoplasmic proteins (cytoplasmic fraction) and the second enriched for axonemal proteins (axonemal fraction). We confirmed enrichment of cytoplasmic proteins with antibody to DNAAF2 (**Fig. 5b**) and of axonemal proteins with antibody to LRRC48 (**Fig. 5b**).

Coimmunoprecipititation assays of epitope-tagged constructs and protein blotting. HEK293 cells were transfected with plasmids encoding Myc- and Flag-tagged proteins using Gene Juice (Novagen) with approximately 0.1 µg/ml DNA in the medium. Within 24 h, cells were collected in 1× PBS and lysed in 1 ml of buffer containing 50 mM Tris-HCl, pH 8.0, 150 mM NaCl, 1% IGEPAL, 0.5 mM EDTA and 10% glycerol supplemented with protease inhibitor cocktail (Roche Complete) and phosphatase inhibitors (Cocktails 2 and 3, Sigma-Aldrich). Lysates were centrifuged at 16,000*g* for 30 min at 4 °C. Approximately 2 mg of each lysate was precleared with 4 µg of rabbit control IgG for 2 h at 4 °C and was incubated with MagSi/protein A beads (MagnaMedics) for 1 h. Lysates were incubated with 4 µg of rabbit antibody to Flag or with antibody to Myc overnight at 4 °C and were then incubated with MagSi/protein A beads for 1 h to capture immunoprecipitates. Bead complexes were washed four times in lysis buffer and were resuspended in 1× LDS buffer supplemented with DTT (1/8 lysis volume) and heated for 10 min at 90 °C. Lysates were electrophoresed in NuPAGE 4–12% Bis-Tris gels, transferred to PVDF membranes and subsequently immunoblotted with mouse monoclonal antibody to either Myc (A7) or Flag (M2). PVDF membranes were washed three times in TBS-T (10 min per wash) before blocking in 5% BSA for 2 h at room temperature. Membranes were then washed three times (10 min per wash) before incubation with primary antibody (diluted in TBS-T) overnight at 4 °C. Membranes were washed three times (10 min per wash) and incubated with secondary antibody for 1 h at room temperature. Membranes were washed four times and developed by ECL using Prime Western Blotting Detection Reagent (Amersham). Images were digitally acquired using a FUSION-SL Advance Imager (PeqLab) and modified for contrast using Adobe Photoshop CS4. All wash and incubation steps were performed with gentle shaking. The following antibodies were used: rabbit polyclonal antibody to DNAAF2 (1:1,000 dilution; Atlas Antibodies, HPA004113), rabbit polyclonal antibody to LRRC48 (1:500 dilution; Atlas Antibodies, HPA036040), rabbit polyclonal antibody to DYX1C1 (1:1,000 dilution; ProteinTech, 14522-1-AP), rabbit polyclonal antibody to Myc (1:25 dilution; clone A-14, Santa Cruz Biotechnology), mouse monoclonal antibody to Myc (1:2,000 dilution; clone A.7, Abcam), rabbit polyclonal control IgG (1:25 dilution; sc-2027, Santa Cruz Biotechnology), rabbit polyclonal antibody to Flag (1:250 dilution; clone F7425, Sigma-Aldrich), mouse monoclonal antibody to Flag (1:2,000 dilution; clone M2, Sigma-Aldrich), HRP-conjugated goat antibody to mouse (1:5,000 dilution; NA931V, GE Healthcare) and HRP-conjugated goat antibody to rabbit (1:3,000 dilution; NA934, GE Healthcare).

Cell culture and transfection. Human embryonic kidney (HEK293T) cells were grown to confluence in DMEM supplemented with 10% FBS, 1% non-essential amino acid (NEAA) and 1% penicillin-streptomycin antibiotics (Invitrogen). Cultures were plated at a density of 5×10^4 cells/well in a 24-well plate. The plasmid constructs used for transfection were pCAG-*Dyx1c1*-GFP, pCAG-*Dyx1c1*-Flag and pCAG-GFP. Before transfection, medium was changed to OptiMEM-1 reduced-serum medium (Invitrogen). DNA (1 µg) was added to each well with 2 µl of Lipofectamine 2000 reagent (Invitrogen) in OptiMEM-1. After incubation of the cells for 6 h at 37 °C, the medium was exchanged for normal growth medium. After a second incubation for 72 h, fluorescence images were obtained by Carl Zeiss Axiovert 200M Inverted microscope with an ApoTome attachment (**Supplementary Fig. 9a–c**). Protein blots were also performed on the transfected cells as described above (**Supplementary Fig. 9d**).

Yeast two-hybrid assays. To analyze the binding capacity between DYX1C1 and DNAAF2, plasmids expressing full-length DYX1C1 fused to a DNA-binding domain (GAL4-BD) and full-length DNAAF2 fused to an activation domain (GAL4-AD) were transformed into yeast strains PJ69-4A and PJ69-4α, respectively. These strains were subsequently combined by yeast mating, and diploids containing both plasmids were selected on medium lacking leucine and tryptophan. Interactions were analyzed by the assessment of reporter gene activation via growth on medium additionally lacking histidine and adenine to detect *HIS3* and *ADE2* reporter gene activation, α-galactosidase colorimetric plate assays (*MEL1* reporter gene, data not shown) and β-galactosidase colorimetric filter lift assays (*LacZ* reporter gene). As a positive control, the binding capacity of the known interactors BD-USH2A_icd and AD-NINL_isoB was assessed, and, as a negative control, the inability of BD-USH2A_icd to bind to only the GAL4 domain (AD-GAL4) was used. Detailed protocols for the evaluation of protein-protein interactions are available from the authors upon request.

47. Wilkinson, D.G. & Nieto, M.A. Detection of messenger RNA by *in situ* hybridization to tissue sections and whole mounts. *Methods Enzymol.* **225**, 361–373 (1993).
48. Doetsch, F. & Alvarez-Buylla, A. Network of tangential pathways for neuronal migration in adult mammalian brain. *Proc. Natl. Acad. Sci. USA* **93**, 14895–14900 (1996).
49. Huang, D.W. *et al.* Systematic and integrative analysis of large gene lists using DAVID bioinformatics resources. *Nat. Protoc.* **4**, 44–57 (2009).
50. Huang, D.W. *et al.* Bioinformatics enrichment tools: paths toward the comprehensive functional analysis of large gene lists. *Nucleic Acids Res.* **37**, 1–13 (2009).
51. Gritsman, K. *et al.* The EGF-CFC protein one-eyed pinhead is essential for nodal signaling. *Cell* **97**, 121–132 (1999).
52. Yelon, D. *et al.* Restricted expression of cardiac myosin genes reveals regulated aspects of heart tube assembly in zebrafish. *Dev. Biol.* **214**, 23–37 (1999).

doi:10.1038/ng.2707

53. Odenthal, J. & Nüsslein-Volhard, C. fork head domain genes in zebrafish. *Dev. Genes Evol.* **208**, 245–258 (1998).
54. Milewski, W.M. *et al.* Conservation of PDX-1 structure, function, and expression in zebrafish. *Endocrinology* **139**, 1440–1449 (1998).
55. Struhl, G. Anterior and posterior compartments in the proboscis of *Drosophila*. *Dev. Biol.* **84**, 372–385 (1981).
56. Zariwala, M.A. *et al.* Genetic defects in ciliary structure and function. *Annu. Rev. Physiol.* **69**, 423–450 (2007).
57. Sisson, J.H. *et al.* All-digital image capture and whole-field analysis of ciliary beat frequency. *J. Microsc.* **211**, 103–111 (2003).
58. Fliegauf, M. *et al.* Mislocalization of DNAH5 and DNAH9 in respiratory cells from patients with primary ciliary dyskinesia. *Am. J. Respir. Crit. Care Med.* **171**, 1343–1349 (2005).
59. Rashid, S. *et al.* The murine *Dnali1* gene encodes a flagellar protein that interacts with the cytoplasmic dynein heavy chain 1. *Mol. Reprod. Dev.* **73**, 784–794 (2006).
60. Olbrich, H. *et al.* Axonemal localization of the dynein component DNAH5 is not altered in secondary ciliary dyskinesia. *Pediatr. Res.* **59**, 418–422 (2006).
61. Reed, W. *et al.* Characterization of an axonemal dynein heavy chain expressed early in airway epithelial ciliogenesis. *Am. J. Respir. Cell Mol. Biol.* **23**, 734–741 (2000).